Chinese Journal of Chemical Engineering 70 (2024) 63–72

Contents lists available at ScienceDirect

Chinese Journal of Chemical Engineering

journal homepage: www.elsevier.com/locate/CJChE

Full Length Article

Experimental and numerical investigations on micromixing performance of multi-orifice cross-flow jet mixers

Hang Yang, Zhaojin Lu, Likun Ma, Wei Yin, Bingjie Wang, Zhishan Bai, Xiaoyong Yang*

School of Mechanical and Power Engineering, East China University of Science and Technology, Shanghai 200237, China

ARTICLE INFO

Article history:
Received 10 October 2023
Received in revised form
16 March 2024
Accepted 18 March 2024
Available online 4 April 2024

Keywords:
Multi-orifice cross-flow jet mixer
Micromixing performance
Finite-rate/modified eddy dissipation model
Computational fluid dynamics
Villermaux/Dushman reaction

ABSTRACT

Multi-orifice cross-flow jet mixers (MOCJMs) are used in various industrial applications due to their excellent mixing efficiency, but few studies have focused on the micromixing performance of MOCJMs. Herein, the flow characteristics and micromixing performance inside the MOCJM were investigated using experiments and computational fluid dynamics (CFD) simulations based on the Villermaux/Dushman system and the finite-rate/modified eddy-dissipation model. The optimal A value was correlated with the characteristic parameters of MOCJMs to develop a CFD calculation method applicable to the study of the micromixing performance of the MOCJMs. Then the micromixing efficiency was evaluated using the segregation index X_S, and the effects of operational and geometric parameters such as mixing flow Reynolds number (Re_M), flow ratio (R_F), total jet area (S_T), the number of jet orifices (n), and outlet configuration on the micromixing efficiency were investigated. It was found that the intensive turbulent region generated by interactions between jets, as well as between jets and crossflows, facilitated rapid reactions. X_S decreased with increasing Re_M and decreasing R_F. Furthermore, MOCJMs with lower S_T, four jet orifices, and the narrower outlet configuration demonstrated a better micromixing efficiency. This study contributes to a deeper understanding of the micromixing performance of MOCJMs and provides valuable guidance for their design, optimization, and industrial application.

1. Introduction

The mixing process holds paramount importance for numerous chemical reactions and production processes. In order to realize rapid mixing of fluids, researchers have developed various forms of jet mixers, including coaxial jet mixers [1], countercurrent jet mixers [2], cross-flow jet mixers [3], and impingement jet mixers [4]. The principle of cross-flow jet mixers involves injecting two or more fluids into a mixing chamber through high-speed jets, facilitating rapid fluid mixing and dispersion through turbulence and molecular diffusion. The cross-flow jet mixer with porous injection is referred to as the multi-orifice cross-flow jet mixer (MOCJM), characterized by its simple structure and high mixing rate. It has been widely used in fields such as crystallization, nano-particle preparation, chlorination processes, combustion, *etc.* [5–8]. Over the past decades, researchers have conducted extensive experimental and simulation work on the mixing mechanism and macroscopic characteristics of MOCJMs. Concerning the mixing mechanism, particular attention has been directed toward the formation and development of cross-flow jet vortex structures [9–13]. The prevailing view is that interactions between jets and crossflows, as well as among jets, generate vortex systems, including counter-rotating vortex pairs, shear layer vortices, horseshoe-shaped vortices encircling jet columns, and wake vortices in the lee of jets. In terms of macroscopic characteristics, research has focused on macromixing performance, flow pattern, and jet trajectories [14–22].

However, to the best of our knowledge, limited research has been dedicated to exploring the micromixing performance inside MOCJMs. For complex fast-reaction systems (such as precipitation, polymerization, crystallization, complex organic synthesis reactions, *etc.*), product yield and selectivity depend not only on macromixing at the reactor scale, but also on micromixing from the smallest tiny elements scale of turbulent dispersion to the molecular scale [23]. Moreover, micromixing efficiency is widely acknowledged as a key indicator for evaluating reactor performance, and many studies have delved into micromixing efficiency in different types of reactors [24–26]. Hence, conducting research on the micromixing performance within MOCJMs holds considerable significance.

* Corresponding author.
E-mail address: xyyang@ecust.edu.cn (X. Yang).

https://doi.org/10.1016/j.cjche.2024.03.007

A lot of methods have been proposed for evaluating micromixing performance. Among them, the chemical reaction method, which uses mixing-sensitive chemical reactions as molecular probes, has distinct advantages compared to traditional physical measurement methods. The chemical reaction method involves introducing a reaction system with known reaction kinetics into the mixer and exploring the micromixing effect by analyzing the conversion of the reactants and selectivity of products after mixing. Based on the Villermaux/Dushman reaction system, researchers have used the chemical reaction method to investigate micromixing in microchannel reactors [27], rotating packed bed reactors [28], helical-tube reactors [29], and several other types of reactors. Nevertheless, it is challenging to obtain fluid-flow information and species concentration distribution using experimental methods and change the geometric shape of reactors to optimize their structure.

In recent years, with the development of computer science, numerical simulations using computational fluid dynamics (CFD) methods have proven to be an effective and economical approach in studying reactive flows. An increasing number of scholars are utilizing CFD simulations to analyze the micromixing performance within reactors. Liu *et al.* [30] used the direct quadrature method of moments combined with the interaction by exchange with the mean to investigate the micromixing performance within a swirling reactor. The results indicated that the introduction of ultrasound can intensify turbulence, leading to a relatively uniform environment for chemical reactions and thus reducing by-products. In a work on coaxial mixers, CFD simulations using the concepts of turbulence dissipation and engulfment models indicated that the micromixing performance of a six-pitched blade/Rushton turbine impeller surpassed that of a six-straight-blade/Rushton turbine impeller when the feeding point was in close proximity to the Rushton turbine impeller [31]. Ouyang *et al.* [24] utilized CFD simulations combined with the finite-rate/modified eddy-dissipation model (FR/MEDM) to investigate the micromixing in a rotating packed bed. The results indicated a high level of consistency between simulation and experimental data. Micromixing efficiency was enhanced with increased liquid-flow rates, reduced viscosity, and higher rotational speeds. This paper used the FR/MEDM because it offers reasonable accuracy and lower computational costs than other methods.

Given the research status quo, this study aims to evaluate the micromixing performance within MOCJMs. Based on the Villermaux/Dushman reaction and the FR/MEDM, the experimental and CFD methods were utilized to explore the internal flow characteristics and reaction processes of the mixer in this work. Effects of various operational parameters and geometric parameters on the micromixing performance were analyzed, and the mechanisms of micromixing intensification of MOCJMs were elucidated.

2. Experimental

2.1. Materials and equipment

Table 1 shows the experimental reagents and initial concentrations of species used for the parallel competitive reactions.

Table 1
Experimental reagents and their initial concentrations

Species	Purity/%	Company	Initial concentrations/mol·L^{-1}
H_3BO_3	99.5	Aladdin	0.1818
NaOH	98.0	Aladdin	0.0909
KI	99.0	Aladdin	0.0160
KIO_3	99.995	Aladdin	0.0033
H_2SO_4	98.0	Aladdin	0.02/0.04/0.08

H_3BO_3 and NaOH were first dissolved in deionized water to prepare a buffer solution. Subsequently, solutions of KI and KIO_3 were prepared and added to the buffer solution to form stream A. H_2SO_4 was dissolved in deionized water to prepare stream B.

Fig. 1 depicts the schematic diagram of the experimental setup and the geometric structure of the 3D-printed MOCJMs. Both stream A and stream B are simultaneously pumped into the jet mixer by a centrifugal pump, with volumetric flow rates ranging from 1 to 5 L·min^{-1}. After mixing inside the MOCJMs, samples of the mixture are collected at the outlet at fixed time intervals and analyzed at 353 nm using an ultraviolet (UV) spectrophotometer (Shimadzu UV-1800, Japan). The mixer consisted of a mixing tube for crossflow and one or more orifices (with a diameter of d) for injection. Stream A (crossflow) directly flowed through the mixing tube, and stream B was injected into the mixing pipe to mix with the cross-flow flow *via* the jet orifices. To explore the impact of various structural parameters on micromixing, multiple mixer configurations were designed as presented in Table 2. For example, M-4Φ2-U represents a mixer with four injection orifices, each with a diameter of 2 mm, and the outlet configuration unchanged.

The Reynolds number for mixed stream is defined as follows:

$$Re_M = du_M\rho/\mu \tag{1}$$

where u_M is the outlet velocity, and the flow ratio R_F is defined as:

$$R_F = Q_B/Q_A \tag{2}$$

where Q_A and Q_B represent the flow rates of stream A and stream B, respectively.

2.2. Parallel competing reaction system

Generally, for slow reactions, there is sufficient time for reactants to mix extensively at the molecular level, and the actual reaction rate is determined by intrinsic reaction kinetics. In contrast, for fast reactions, the reaction has occurred before thorough mixing is achieved, leading to side reactions when local concentrations are heterogeneous. In such instances, micromixing processes control the actual reaction rate. To investigate liquid micromixing efficiency within reactors, the Villermaux/Dushman parallel competing reaction system was commonly used. This system is illustrated by reactions (R1) to (R3), representing a three-reaction system.

$$H_2BO_3^- + H^+ \rightarrow H_3BO_3 \tag{R1}$$

$$5I^- + IO_3^- + 6H^+ \rightarrow 3I_2 + 3H_2O \tag{R2}$$

$$I_2 + I^- \rightleftharpoons I_3^- \tag{R3}$$

The neutralization reaction (R1) is a quasi-instantaneous reaction, whereas the oxidation–reduction reaction (R2) is a fast reaction but much slower than reaction (R1), and both of these reactions compete for H^+ [32,33]. If micromixing is perfect, only reaction (R1) occurs. If micromixing is imperfect, an excess of H^+ leads to reaction (R2), resulting in the formation of I_2. Subsequently, I_2 reacts with I^- through reaction (R3) to generate I_3^-. At 25 °C, the kinetic parameters of the parallel competitive reaction system are shown in Table 3, with the kinetics of reaction (R2) depending on ionic strength. The micromixing performance can be evaluated using the segregation index X_S within the range of 0–1, which is defined by the following equations:

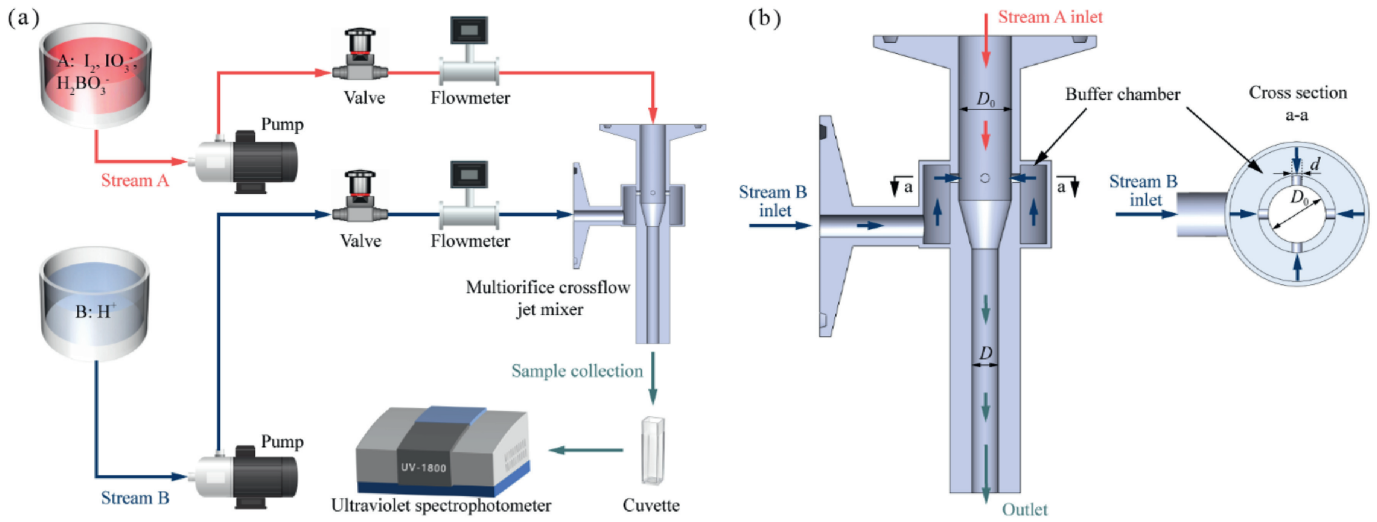

Fig. 1. (a) Experimental setup for parallel competitive reactions. (b) Schematic diagram of MOCJM structure.

Table 2
Geometric parameters of different MOCJMs

Jet mixer	Jet orifices' number n	Jet orifices diameter d/mm	Inner diameter of outlet D/mm	Outlet type
M-4Φ1-U	4	1	12	Unchanged
M-4Φ1.5-U	4	1.5	12	Unchanged
M-4Φ2-U	4	2	12	Unchanged
M-4Φ2.5-U	4	2.5	12	Unchanged
M-4Φ3-U	4	3	12	Unchanged
M-1Φ4-U	1	4	12	Unchanged
M-2Φ2.83-U	2	2.83	12	Unchanged
M-8Φ1.41-U	8	1.41	12	Unchanged
M-4Φ2-N	4	2	6	Narrowed
M-4Φ2-E	4	2	18	Enlarged

Table 3
Parallel competing reaction kinetic parameters [34]

Reaction	Kinetics	k
(R1)	$r_1 = k_1[H^+][H_2BO_3^-]$	$k_1 = 10^{11}\ m^3\cdot kmol^{-1}\cdot s^{-1}$
(R2)	$r_2 = k_2[H^+]^2[I^-]^2[IO_3^-]$	$[I] < 0.166\ mol\cdot L^{-1}, \lg(k_2) = 9.28105 - 3.664\sqrt{[I]}$
		$[I] > 0.166\ mol\cdot L^{-1}, \lg(k_2) = 8.383 - 1.5112\sqrt{[I]} + 0.23689[I]$
(R3)	$r_3 = k_{3+}[I^-][I_2] - k_{3-}[I_3^-]$	$k_{3+} = 5.9 \times 10^9\ m^3\cdot kmol^{-1}\cdot s^{-1}$
		$k_{3-} = 7.5 \times 10^9\ s^{-1}$

$$X_S = \frac{Y}{Y_{ST}} \tag{3}$$

$$Y = \frac{2(V_A + V_B)([I_2] + [I_3^-])}{V_A[H^+]_0} \tag{4}$$

$$Y_{ST} = \frac{6[IO_3^-]_0}{6[O_3^-]_0 + [H_2BO_3^-]_0} \tag{5}$$

The value of X_S ranges from 0 to 1. $X_S = 0$ is for perfectly micromixing, whereas $X_S = 1$ is for absolute segregation. A smaller X_S indicates a better micromixing performance.

3. Computational Fluid Dynamics Model

3.1. Governing equations

The simulation assumed that the fluid in MOCJM was incompressible single-phase flow, with the governing equations as follows:

Continuity equation:

$$\nabla \cdot \boldsymbol{u} = 0 \tag{6}$$

Momentum conservation equations:

$$\rho \boldsymbol{u} \cdot \nabla \boldsymbol{u} = -\nabla \boldsymbol{p} + \mu \nabla^2 \boldsymbol{u} \tag{7}$$

Species transport equation:

$$\rho\nabla\cdot(\boldsymbol{u}y_i)=\rho\nabla\cdot\left[\left(D_i+\frac{\mu_t}{Sc_t}\right)\nabla y_i\right]+R_i \tag{8}$$

In the aforementioned equations, y_i represents the local mass fraction of species i, D_i is the mass diffusion coefficient of species i, whereas μ_t and Sc_t denote turbulent viscosity and turbulent Schmidt number, respectively. R_i stands for the net rate of species i resulting from chemical reactions. In comparison with the standard k–ε model, the realizable k–ε model introduces strain and rotation tensors into the calculation of turbulent viscosity, and constraints are applied to the Reynolds stress in the realizable k–ε turbulence model to make the model more consistent with turbulent flow physics, enabling more accurate prediction of round jets. Additionally, accurate predictions of the flow field and concentration field of multi-orifice cross-flow jet have been obtained by using the realizable k–ε model [3,13]. Large eddy simulation requires more computational cost than the Reynolds-averaged Navier–Stokes (RANS) model with the same structure and number of meshes. Hence, considering computational capability and accuracy, the RANS model with realizable k–ε turbulence equations was adopted in this paper:

$$\rho\nabla(\boldsymbol{u}k)=\nabla\left[\left(\mu+\frac{\mu_t}{\sigma k}\right)\nabla k\right]+\mu_t\nabla\boldsymbol{u}\left(\nabla\boldsymbol{u}+\nabla\boldsymbol{u}^{\mathrm{T}}\right)-\rho\varepsilon \tag{9}$$

$$\rho\nabla(\boldsymbol{u}\varepsilon)=\nabla\left[\left(\mu+\frac{\mu_t}{\sigma_\varepsilon}\right)\nabla\varepsilon\right]+C_{1\varepsilon}S\rho\varepsilon-\frac{C_{2\varepsilon}}{k+\sqrt{\nu\varepsilon}}\rho\varepsilon^2 \tag{10}$$

The definition of turbulent viscosity is as follows:

$$\mu_t=\rho C_\mu\frac{k^2}{\varepsilon} \tag{11}$$

where

$$C_\mu=\frac{1}{4.04+\sqrt{6S_{ij}S_{ij}}\left(k/t\right)\cos\varphi}\quad,\ \varphi=\frac{1}{3}\cos^{-1}\frac{\sqrt{6}S_{ij}S_{jk}S_{ki}}{\left(S_{ij}S_{ij}\right)^{3/2}} \tag{12}$$

$$S=\sqrt{2S_{ij}S_j}\ ,S_{ij}=\frac{1}{2}\left(\frac{\partial u_j}{\partial x_i}+\frac{\partial u_i}{\partial x_j}\right) \tag{13}$$

In these equations, $C_{1\varepsilon}$ and $C_{2\varepsilon}$ are constant, and σ_k and σ_ε represent the turbulent Prandtl numbers for k and ε. The default values in ANSYS FLUENT were used in the simulation: $C_{1\varepsilon}=1.44$; $C_{2\varepsilon}=1.9$; $\sigma_k=1.0$; $\sigma_\varepsilon=1.2$.

3.2. Finite-rate/modified eddy-dissipation model

In the finite-rate/eddy-dissipation model, the reaction rate is controlled by intrinsic kinetics and turbulent mixing, and the net reaction rate is determined as the smaller value between the Arrhenius rate and the eddy-dissipation reaction rate. For the finite-rate model, the molar reaction rate of species i is calculated by the following equation:

$$R_{i,r}^{r}=\left(\nu_{i,r}^{''}-\nu_{i,r}^{'}\right)\left[k_{f,r}\prod_{j=1}^{N}\left(C_{j,r}\right)^{m}-k_{b,r}\prod_{j=1}^{N}\left(C_{j,r}\right)^{n}\right] \tag{14}$$

where $C_{j,r}$ represents the concentration of species j participating in reaction r, m and n represent the exponents of reactants and products, respectively, $k_{f,r}$ and $k_{b,r}$ represent the rate constants for the forward and reverse reactions, respectively, $\nu_{i,r}^{'}$ and $\nu_{i,r}^{''}$ stand for the stoichiometric coefficients of reactant and product i in reaction r, respectively. The eddy-dissipation model was originally used in numerical simulations of combustion processes, which involve extremely fast reactions. A reasonable assumption is that the reaction rate is controlled by the mixing rate rather than reaction kinetics. Based on this assumption, the reaction rate of component i can be calculated using Eq. (15).

$$R_{i,r}^{t}=\nu_{i,r}^{'}M_iA\rho\frac{\varepsilon}{k}\min\left[\min_R\left(\frac{Y_R}{\nu_{R,r}^{'}M_R}\right),\frac{B\sum_P Y_P}{\sum_j^N\nu_{j,r}^{''}M_j}\right] \tag{15}$$

where Y_R and Y_P represent the mass fractions of reactant R and product P, respectively, whereas M_i and M_j denote the molecular weights of reactants and products. A and B are empirical constants associated with simulating flame diffusion and spread. However, for liquid-phase fast chemical reactions, the value of A is related to turbulence intensity, and the value of B should be neglected [35]. The turbulent Reynolds number, as given in Eq. (16), can be used to describe the intensity of turbulence. For different reaction processes and experimental conditions, there exists an optimal value for A. Wang [36] conducted a systematic study on the optimal A value and correlated it with Re_t:

$$Re_t=\frac{u'l}{\nu}=\frac{0.816k^{1/2}\left(0.164k^{2/3}/\varepsilon\right)}{\nu}=0.134\frac{k^2}{\nu\varepsilon} \tag{16}$$

Here, ν represents the kinematic viscosity. Therefore, the modified eddy-dissipation model is expressed by the following equation:

$$R_{i,r}^{t}=\nu_{i,r}^{'}M_iA\rho\frac{\varepsilon}{k}\min_R\left(\frac{Y_R}{\nu_{R,r}^{'}M_R}\right)=\nu_{i,r}^{'}M_if(Re_t)\rho\frac{\varepsilon}{k}\min_R\left(\frac{Y_R}{\nu_{R,r}^{'}M_R}\right) \tag{17}$$

Therefore, the FR/MEDM can be expressed by the following equation:

$$R_{i,r}=\min\left(R_{i,r}^{r},R_{i,r}^{t}\right) \tag{18}$$

3.3. Physical models and boundary conditions

Steady RANS simulations were performed using FLUENT software with a double-precision model. The viscosity model used the realizable k–ε model. The reactions were modeled using the species transport equation and the finite-rate/improved eddy-dissipation model, with volumetric reaction rate simulating reaction kinetics. It was assumed that the physical properties of solution A and solution B were the same as those of water at 298.15 K, with a density ρ of 998.2 $kg\cdot m^{-3}$ and a dynamic viscosity μ of 10^{-3} $Pa\cdot s$. The diffusion coefficients for each species were set as 10^{-9} $m^2\cdot s^{-1}$. Velocity inlet, pressure outlet, and no-slip-wall boundary conditions were set. The pressure–velocity coupling was addressed using the semi-implicit method for pressure-linked equations (SIMPLE) algorithm, and gradient and pressure discretization were performed using the Green–Gauss cell-based and PRESTO methods, whereas the remaining terms were solved with second-order upwind schemes. The calculations were iteratively repeated until the numerical solutions of all equations met a convergence criterion of at least 10^{-5}.

Fig. 2(a) illustrates the schematic diagram of the hexahedral structured grid partitioned using ICEM software. To validate grid independence, four grids of different sizes were generated. As shown in Fig. 2(b), when the number of grids increases to 564027, the mass fraction distribution of I_2 hardly changes, indicating that

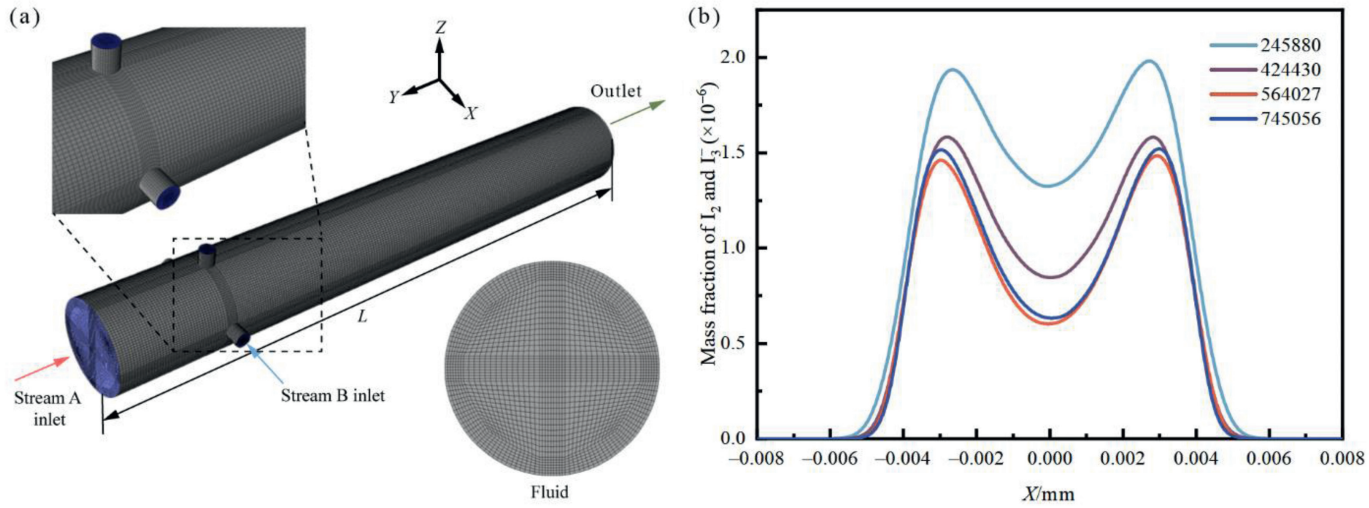

Fig. 2. (a) Hexahedral structured mesh; (b) mass fraction of I_2 and I_3^- along the X axis of the MOCJM.

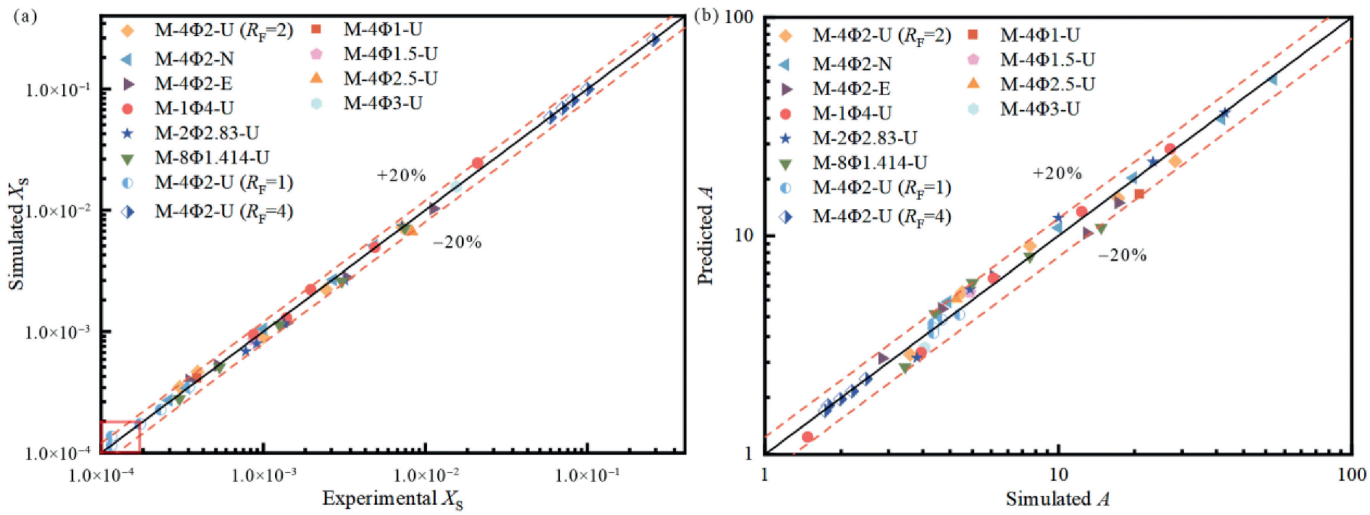

Fig. 3. (a) Comparison of X_S between experimental data and numerical values; (b) comparison of A between experimental data and predicted value.

Table 4
The correlation between A and characteristic parameters of MOCJMs

Configuration	Operational parameters	Correlation of the optimal A
M-4Φ2-U, M-4Φ1-U, M-4Φ1.5-U, M-4Φ2-U, M-4Φ2.5-U, M-4Φ3-U, M-1Φ4-U, M-2Φ2.83-U, M-8Φ1.41-U, M-4Φ2-N, M-4Φ2-E, M-4Φ2-U	$R_F = 1$, $[H^+] = 0.04$ mol·L^{-1} $R_F = 2$, $[H^+] = 0.08$ mol·L^{-1} $R_F = 4$, $[H^+] = 0.16$ mol·L^{-1}, $Re_M = 3536–10610$	$A = \left(4.794R_F^2 - 17.772R_F + 21.47\right) \times Re_t^{\left(-2.63R_F^2+13R_F-10.698\right)} n^{0.474}$

grid independence has been achieved. Therefore, subsequent calculations in this paper were carried out using 564027 grids.

4. Results and Discussion

4.1. Validation of simulation and calibration of empirical constant A

In general, the empirical constant A is subject to variations depending on the specific reactor types and operational conditions. Therefore, it is necessary to calibrate the value of A based on experimental results. As shown in Fig. 3(a), the simulated values of X_S agreed well with the experimental data, with a maximum deviation of 19.7% and an average deviation of 7.19%, demonstrating the accuracy of the simulation results. In addition, the optimal A value was correlated with Re_t, R_F and n, as shown in Table 4. Fig. 3(b) indicates good agreement between the simulated and predicted values of A, with a maximum deviation of 21.9% and an average deviation of 9.5%. Therefore, the obtained correlation can provide a feasible method for numerical simulation studies of the flow characteristics, reactions, and micromixing of MOCJMs.

4.2. Flow patterns inside multi-orifice cross-flow jet mixers

The flow patterns within MOCJMs are primarily influenced by the flow ratio [12,18]. Fig. 4 illustrates velocity, streamline, and turbulent kinetic energy distributions in MOCJMs under different

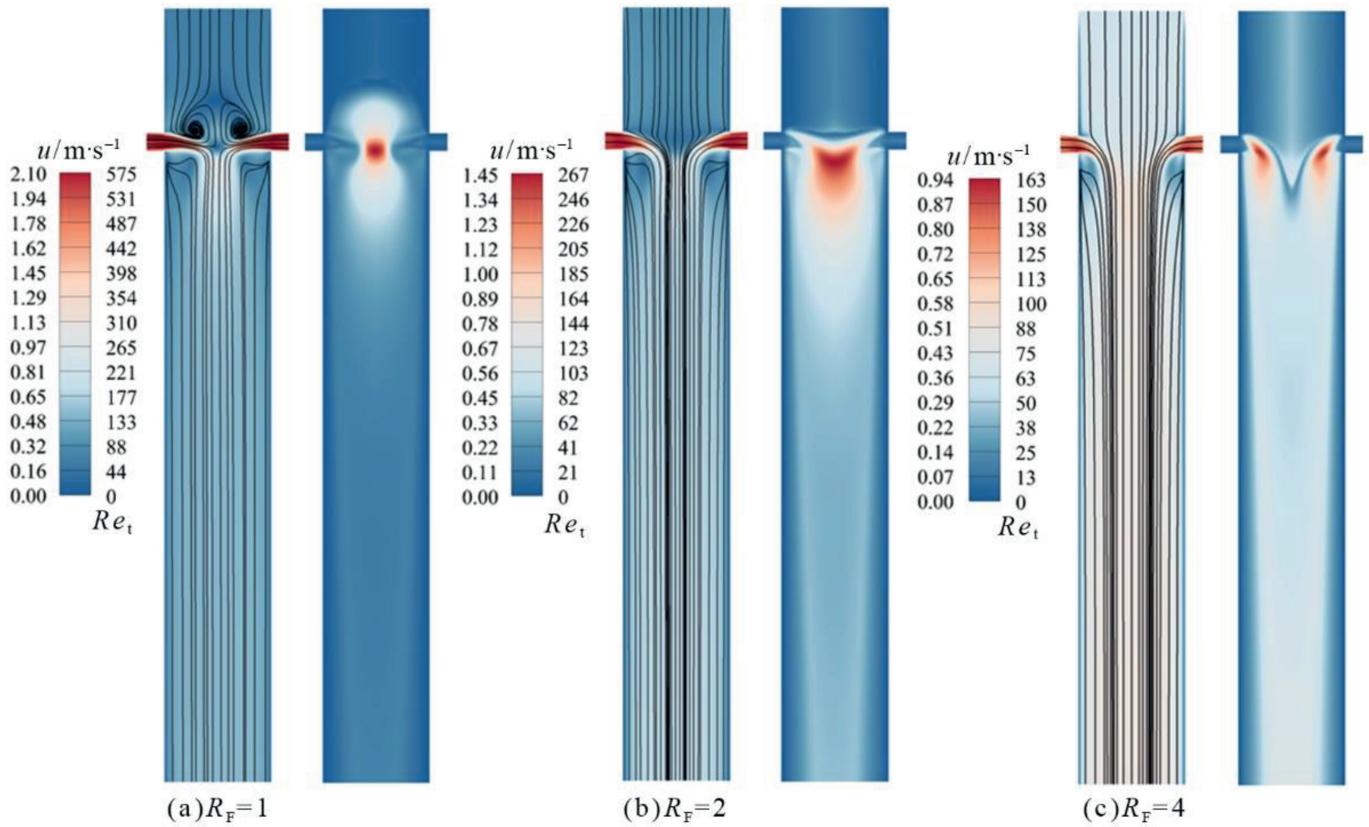

Fig. 4. Velocity, turbulent kinetic energy contours and streamlines at the $Z = 0$ plane of the reactor: (a) $R_F = 1$; (b) $R_F = 2$; (c) $R_F = 4$.

flow ratios. Stream B was injected radially from the jet orifice, mixing with stream A, leading to the rapid generation and dissipation of turbulent kinetic energy. When $R_F = 1$, the impingement among the radial jets at the axis region caused intense turbulent kinetic energy dissipation, with a maximum Re_t of 575. Streamlines indicate the formation of vortices in the upstream region. Some of the mainstream flow deflected toward the reactor wall and was captured by the radial jets to the central axis region, whereas another part flowed downstream through gaps between adjacent radial jets. As the R_F increased to 2, the flow pattern underwent a transition, with no impingement of the radial jet and reduced turbulence in the upstream region. When R_F reached 4, the core of the radial jet was adjacent to the mixer wall, resulting in a significant reduction in turbulence intensity.

Fig. 5 presents the mass fraction contours of various species simulated in MOCJM at different flow ratios. Since reaction (R1) is quasi-instantaneous, most of the H^+ was rapidly neutralized by $H_2BO_3^-$ to form H_3BO_3. Reaction (R2) consumed only a small amount of H^+ to form I_2. In the case of perfect micromixing, only reaction (R1) occurs, and no I_2 is generated. However, if micromixing is imperfect, the local excess of H^+ leads to the occurrence of reaction (R2), resulting in the formation of I_2. As shown in Fig. 5, H^+ was rapidly consumed, and the concentrations of $H_3BO_3^-$ and I_2 became uniform at the outlet.

4.3. Effect of Reynolds number and volume flow ratio on X_S

Fig. 6(a) illustrates that X_S decreased with increasing Re_M. This was due to the higher turbulence intensity in the mixing zone at higher Re_M, resulting in much more tiny elements of acid solution, implying a larger contact area and higher micromixing efficiency [37]. To investigate the effect of the flow ratio on X_S, the total flow rate was kept constant, and the flow rates of streams A and B were adjusted (changing the H^+ concentration in stream B to maintain $n_A/n_B = Q_A C_{A0}/Q_B C_{B0} =$ constant). The results indicated that the flow ratio significantly affects the micromixing process, with X_S decreasing as the flow ratio decreases, reaching a minimum at $R_F = 1$. This implies that smaller flow ratios result in higher micromixing efficiency. At $R_F = 4$, X_S was significantly higher than at $R_F = 1$ and 2. This is because the absence of jet impingement results in very low turbulence intensity, leading to a reduced reaction rate of (R1) and weaker competition for H^+, allowing more H^+ to participate in (R2). As the flow ratio decreased to 2, the increase in radial jet velocity enhanced the entrainment efficiency of the radial jet, promoting the contact between the two streams, and the increase in radial jet depth resulted in a more uniform radial distribution of species. Additionally, the impact between the main stream and the radial jet was intensified, increasing turbulence kinetic energy, thereby reducing the X_S. When $R_F = 1$, X_S further decreased. This can be attributed to the high turbulence intensity generated by impingement among jets and the formation of upstream eddies. Besides, the bigger volume difference between the two streams at higher R_F required a longer time for uniform mixing, resulting in a decrease in micromixing efficiency.

Fig. 6(b) illustrates the distribution of X_S along the axial channel. The results indicated that X_S increased with the axial distance L. There existed a characteristic region of rapid X_S increased between 9 and 26 mm, whereas X_S exhibited minimal changes in other regions. This suggests that the mixing and reaction processes primarily occur within the characteristic region, which serves as the contact zone where stream A and stream B converge in an MOCJM. The interactions among jet flows, between jet flows and

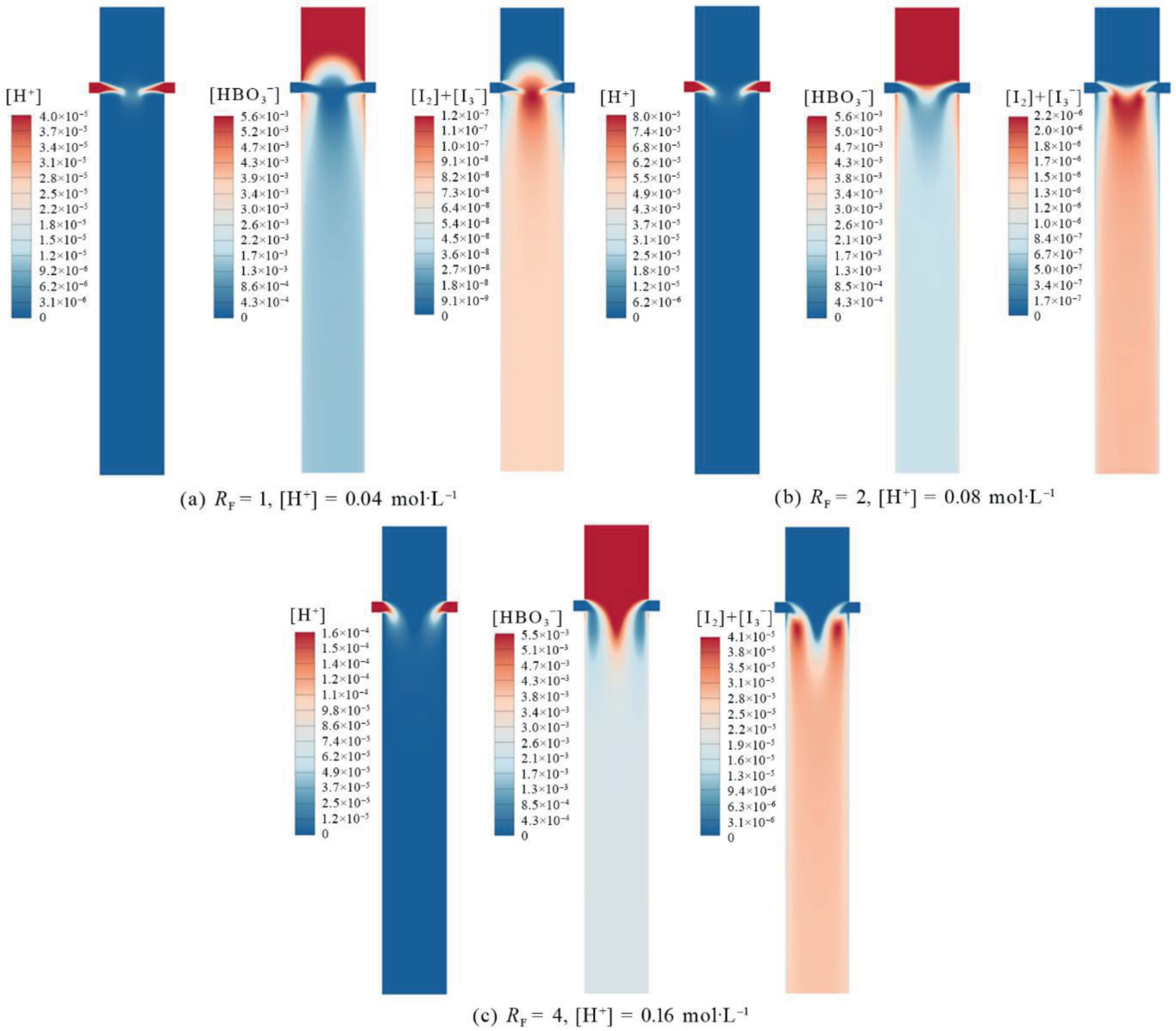

Fig. 5. Mass fraction contours of various species at $Z = 0$ plane for different flow ratios: (a) $R_F = 1$, $[H^+] = 0.04$ mol·L^{-1}; (b) $R_F = 2$, $[H^+] = 0.08$ mol·L^{-1}; (c) $R_F = 4$, $[H^+] = 0.16$ mol·L^{-1}.

mainstream, resulted in intense turbulent energy dissipation, leading to the rapid increase of I_2 and I_3^- due to heterogeneous mixing. In addition, the length of the mixer can be reduced in practical applications because the length of the mixer has a negligible effect on the X_S. For $R_F = 1$, the liquid entered the characteristic region at $L = 9$ mm, whereas for other flow ratios, the liquid entered this region at $L = 14$ mm, which can be explained by the formation of upstream vortices.

4.4. Effect of total jet area on X_S

To explore the influence of the total jet area on X_S, the total flow rate, flow ratio, and jet orifices' number were held constant, whereas the hole diameter was varied ($d = 1, 1.5, 2, 2.5, 3$ mm). Fig. 7(a) reveals that X_S decreased with the reduction in the total jet area. As shown in Fig. 7(b), when the jet area was large, the jet velocity was low, and the depth of the jet was insufficient, resulting in no jet impingement in the central region, leading to low turbulence. When the jet area decreased to 7.07 mm^2, radial jets impinged at the central axis region, leading to the generation of upstream vortices and a noticeable increase in turbulence levels, facilitating the formation of smaller acid solution tiny elements. With further reduction in the jet area, the upstream vortex area expanded, and more turbulent energy dissipated in the central impingement zone, promoting intense mixing and molecular diffusion.

4.5. Effect of jet orifices' number on X_S

Fig. 8 illustrates the influence of the jet orifices' number on X_S and Re_t distributions, within a Re_M range from 3536 to 10610. By changing the number of jet orifices from 1 to 8, while keeping the total jet area constant and varying the orifice diameter from 1 mm

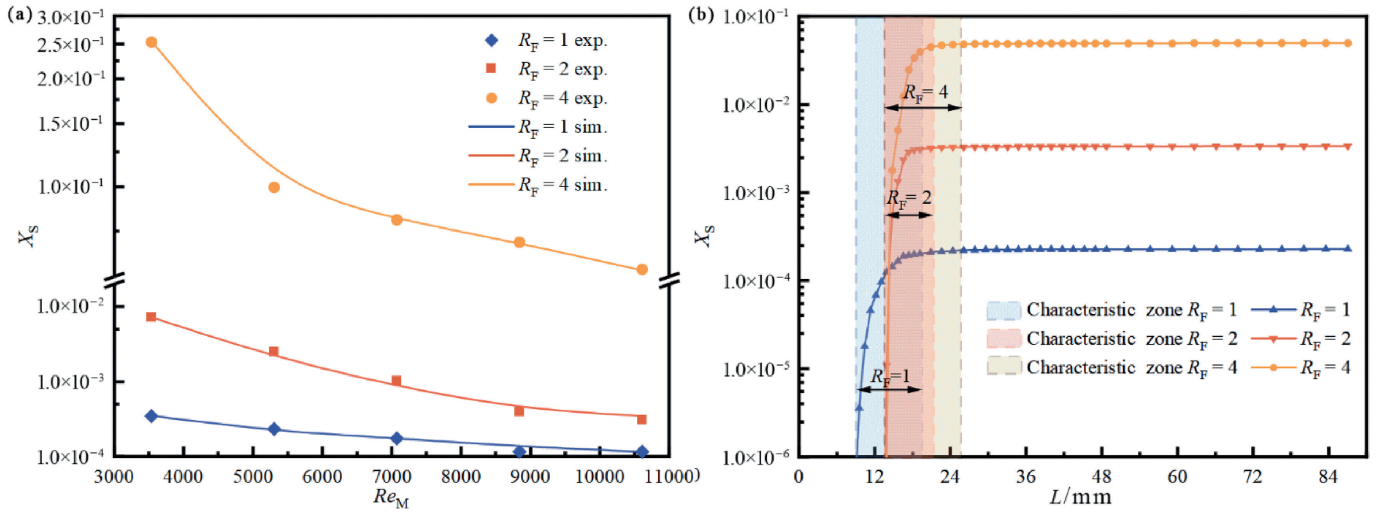

Fig. 6. (a) Effects of R_F and Re_M on X_S inside M-4Φ2-U (Re_M = 7073); (b) effects of mixer length on X_S simulated in M-4Φ2-U.

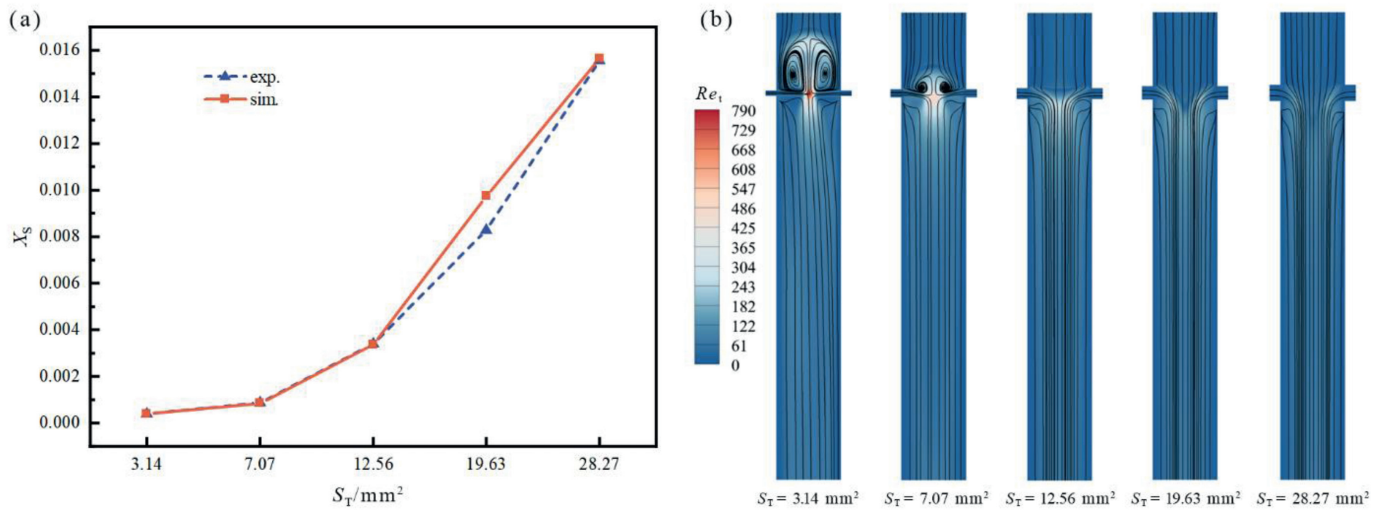

Fig. 7. (a) Effect of the total jet area on X_S; (b) Re_t contours for different S_T at Z = 0 plane.

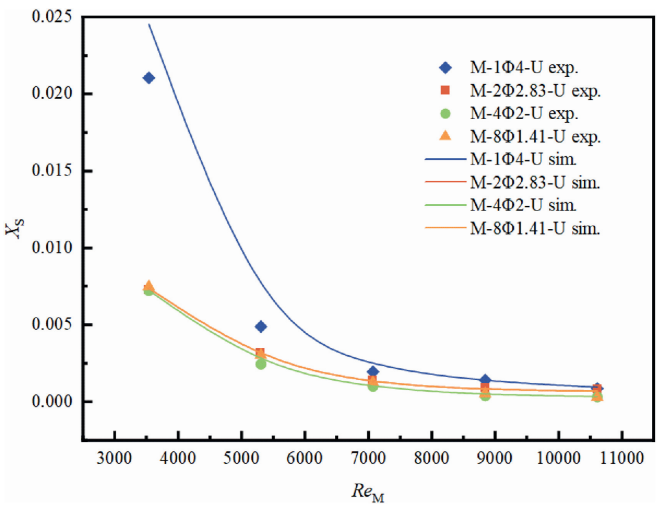

Fig. 8. Effects of jet orifice number on X_S.

to 2.8 mm, it was observed that X_S reached its maximum when n = 1, which can be attributed to lower turbulence intensity. When n = 2, radial jet flows impinged near the central axis, resulting in high turbulence intensity (Fig. 9(a)) and an increase in the number of vortices (Fig. 9(b)). This promoted an increase in the reaction rate of reaction (R1) and improved the macromixing uniformity, leading to higher micromixing efficiency. As n increased to 4, the impingement between jets diminished, causing a reduction in turbulence intensity. However, an increase in the number of vortices leaded to more uniform dispersion of stream B and smaller orifice diameters, resulting in smaller initial dispersion sizes and larger contact area between the continuous and dispersed phases, thus reducing X_S. When n further increased to 8, despite the increased number of vortices and contact area, significant reduction in turbulence intensity resulted in lower micromixing efficiency. Therefore, it can be concluded that the optimal micromixing efficiency was achieved when n = 4, which was determined by the interaction between the jets and crossflow, impingement among the jets, and the contact area between the two phases.

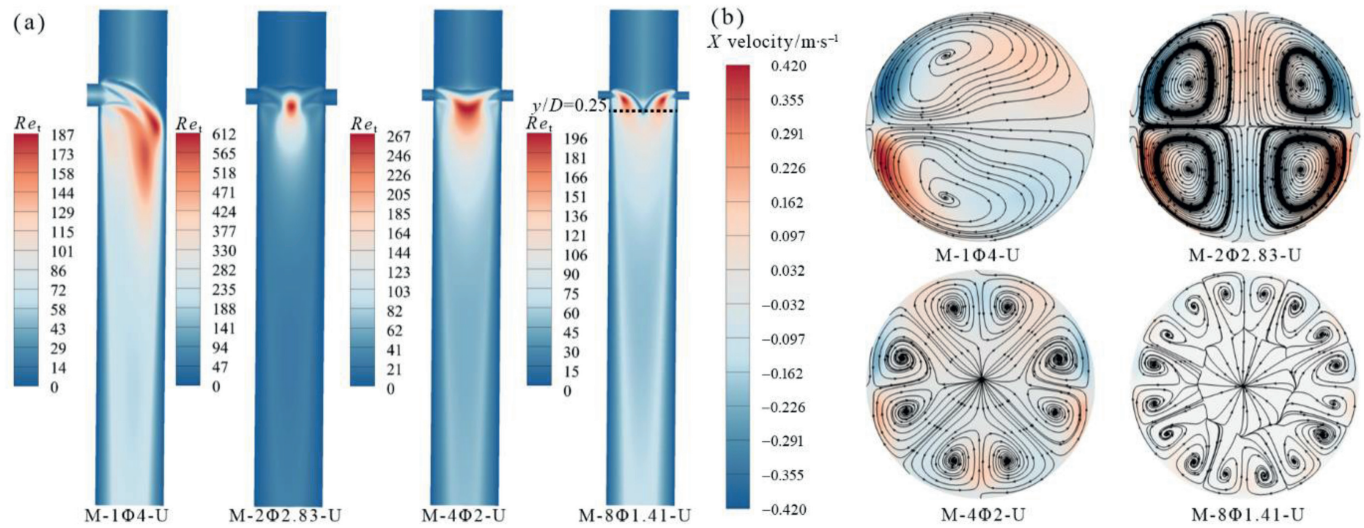

Fig. 9. (a) Re_t contours for different orifice number at $Z = 0$ plane; (b) X velocity and the streamlines at $y/D = 0.25$ plane.

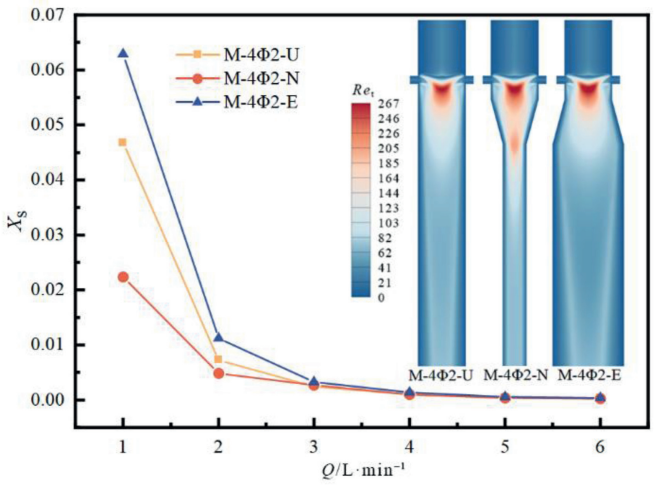

Fig. 10. Effects of outlet configuration on X_S measured experimentally.

4.6. *Effect of outlet configuration on X_S*

As shown in Fig. 10, the micromixing performance of MOCJM with unchanged outlet, narrowed outlet, and enlarged outlet was studied while maintaining the total flow rate. The results indicate that X_S decreased in the order of M-4Φ2-U, M-4Φ2-N, and M-4Φ2-E. The turbulent Reynolds number contours reveal that while the highest turbulence energy was similar in all three types of mixers, the high-energy-dissipation zone occupied a larger percentage of the entire mixer volume in the narrowed mixer, leading to a decrease in segregation scales and segregation intensities of system. Therefore, the reactor with the narrowed outlet configuration exhibited the best micromixing performance, followed by the mixer with an unchanged outlet configuration, and finally the mixer with an enlarged outlet configuration.

5. Conclusions

Based on the Villermaux/Dushman system and the FR/MEDM micromixing model, the flow characteristics and micromixing behaviors inside MOCJMs were investigated in this study using experiments and CFD numerical simulations. The main conclusions are as follows:

(1) CFD simulation results exhibited excellent agreement with experimental data, with a deviation in X_S of less than 20%. Then a CFD method suitable for studying the micromixing performance of MOCJM was developed by correlating the optimal A value with characteristic parameters within a broad range of mixing-flow Reynolds numbers ($Re_M = 3536–10610$).

(2) The effect of operational parameters on X_S were investigated. The segregation index X_S decreased with increasing Re_M. Micromixing efficiency was significantly intensified when the flow rate of the two streams were equal due to the impingement among jet flows and the formation of reverse vortices.

(3) The micromixing performance of MOCJM was mainly influenced by the total jet area, the number of orifices, and the outlet configuration, while being less affected by the mixer length. A smaller total jet area increased the jet flows velocity, causing the jets to collide near the central axis, thereby reducing X_S. With the total jet area held constant, the optimal number of jet orifices existed due to impingement among jet flows, interactions between jet flows and crossflow, and variations in contact area. In the narrowed mixer, an increased percentage of high-turbulence-dissipation zone occupied the total volume-enhanced micromixing efficiency.

Through this work, it is highly desired to provide computational methods and theoretical foundations for the design and structural optimization of MOCJM, promoting its broader application in the field of fast chemical reactions.

CRediT Authorship Contribution Statement

Hang Yang: Investigation, Methodology, Writing – original draft, Writing – review & editing. Zhaojin Lu: Writing – review & editing. Zhishan Bai: Conceptualization, Funding acquisition, Methodology. Xiaoyong Yang: Conceptualization, Formal analysis, Writing – review & editing. Bingjie Wang: Resources, Software. Wei Yin: Project administration, Supervision. Likun Ma: Funding acquisition, Methodology.

Declaration of Interest

The authors declare that they have no known competing financial interests or personal relationships that could have appeared to influence the work reported in this paper.

Acknowledgements

We gratefully acknowledge the financial support from the Shanghai Sailing Program, China (21YF1409500), the National Natural Science Foundation of China (22308100, 22308105), the State Key Laboratory of Chemical Engineering (SKL-ChE-23Z01), and the National Science Fund for Distinguished Young Scholars of China (22225804).

References

[1] A. Giannadakis, A. Naxakis, A. Romeos, K. Perrakis, T. Panidis, An experimental study on a coaxial flow with inner swirl: Vortex evolution and flow field mixing attributes, *Aerosp. Sci. Technol.* 94 (2019) 105373.
[2] K. Wawrzak, A. Boguslawski, Self-excited oscillations in variable density counter-current round jets, *Int. J. Heat Fluid Flow* 103 (2023) 109178.
[3] M.F. Zhou, H. Jiang, Y.J. Hu, Z.M. Lu, H.B. Jiang, C.Z. Li, Analyzing of mixing performance determination factors for the structure of radial multiple jets-in-crossflow, *Chin. J. Chem. Eng.* 27 (11) (2019) 2626–2634.
[4] Y. Liu, R.O. Fox, CFD predictions for chemical processing in a confined impinging-jets reactor, *AIChE J.* 52 (2) (2006) 731–744.
[5] B. Wu, Y. Fang, C.C. Zhao, Y.H. Wang, P.C. Luo, Experimental study and numerical simulation of barium sulfate precipitation process in a continuous multi-orifice-impinging transverse jet reactor, *Powder Technol.* 321 (2017) 180–189.
[6] C.A. da Rosa, R.D. Braatz, Multiscale modeling and simulation of macromixing, micromixing, and crystal size distribution in radial mixers/crystallizers, *Ind. Eng. Chem. Res.* 57 (15) (2018) 5433–5441.
[7] Y.D. Li, Z.F. Nie, Y.Q. Hou, G. Xie, L. Tian, Parametric study of flow field and mixing characteristics of $TiCl_4$ jet injected into O_2 crossflow in oxidation reactor for titanium pigment production by chloride process, *Int. J. Therm. Sci.* 156 (2020) 106460.
[8] X.Y. Yang, W.J. Fan, R.C. Zhang, Experimental investigations on aviation kerosene multi-jets in high temperature and low pressure air crossflow, *Fuel* 324 (2022) 124828.
[9] L. Gevorkyan, T. Shoji, D.R. Getsinger, O.I. Smith, A.R. Karagozian, Transverse jet mixing characteristics, *J. Fluid Mech.* 790 (2016) 237–274.
[10] L.W. Zhang, V. Yang, Flow dynamics and mixing of a transverse jet in crossflow: Part I: Steady crossflow, *J. Eng. Gas Turb. Power* 139 (8) (2017) 082601.
[11] K. Mahesh, The interaction of jets with crossflow, *Annu. Rev. Fluid Mech.* 45 (2013) 379–407.
[12] P.C. Luo, Y. Fang, B. Wu, H. Wu, Turbulent characteristics and design of transverse jet mixers with multiple orifices, *Ind. Eng. Chem. Res.* 55 (32) (2016) 8858–8868.
[13] Z.W. Li, W.X. Huai, Z.D. Qian, Study on the flow field and concentration characteristics of the multiple tandem jets in crossflow, *Sci. China Technol. Sci.* 55 (10) (2012) 2778–2788.
[14] M.T. Kandakure, V.C. Patkar, A.W. Patwardhan, J.A. Patwardhan, Mixing with jets in cross-flow, *Ind. Eng. Chem. Res.* 48 (2009) 6820–6829.
[15] D.J. Clayton, W.P. Jones, Large eddy simulation of impinging jets in a confined flow, in: W. Rodi, M. Mulas (Eds.), Engineering Turbulence Modelling and Experiments 6, Elsevier, Amsterdam, 2005, pp. 247–256.
[16] L.J. Forney, N. Nafia, H.X. Vo, Optimum jet mixing in a tubular reactor, *AIChE J.* 42 (11) (1996) 3113–3122.
[17] D. Liscinsky, B. True, J. Holdeman, Experimental investigation of crossflow jet mixing in a rectangular duct, in: Proceedings of the 29th Joint Propulsion Conference and Exhibit. Monterey, CA, USA, AIAA, Reston, Virigina, 1993, pp. 1993–2037.
[18] P.C. Luo, H.Y. Jia, C.X. Xin, G.Z. Xiang, Z. Jiao, H. Wu, An experimental study of liquid mixing in a multi-orifice-impinging transverse jet mixer using PLIF, *Chem. Eng. J.* 228 (2013) 554–564.
[19] E.V. Kartaev, V.A. Emelkin, M.G. Ktalkherman, S.M. Aulchenko, S.P. Vashenko, V.I. Kuzmin, Formation of counter flow jet resulting from impingement of multiple jets radially injected in a crossflow, *Exp. Therm. Fluid Sci.* 68 (2015) 310–321.
[20] P.C. Luo, Y.C. Tai, Y. Fang, H. Wu, Mixing times in single and multi-orifice-impinging transverse (MOIT) jet mixers with crossflow, *Chin. J. Chem. Eng.* 24 (7) (2016) 825–831.
[21] D.B. Mosiria, R.F. Huang, C.M. Hsu, Characteristics of backward-inclined non-premixed jet flames in crossflow, *Exp. Therm. Fluid Sci.* 98 (2018) 429–444.
[22] Z.W. Li, Y.X. Yuan, J. Yao, V.L. Varsegov, P.H. Duan, L. Zhao, Study of circular transverse jet – A new method for high-efficiency mixing and combustion in crossflow, *Int. Commun. Heat Mass Transf.* 123 (2021) 105207.
[23] J.R. Bourne, Mixing and the selectivity of chemical reactions, *Org. Process Res. Dev.* 7 (4) (2003) 471–508.
[24] Y. Ouyang, Y. Xiang, X.Y. Gao, H.K. Zou, G.W. Chu, R.K. Agarwal, J.F. Chen, Micromixing efficiency optimization of the premixer of a rotating packed bed by CFD, *Chem. Eng. Process. Process. Intensif.* 142 (2019) 107543.
[25] Y. Ouyang, Y. Xiang, H.K. Zou, G.W. Chu, J.F. Chen, Flow characteristics and micromixing modeling in a microporous tube-in-tube microchannel reactor by CFD, *Chem. Eng. J.* 321 (2017) 533–545.
[26] J.Z. Luo, Y. Luo, G.W. Chu, M. Arowo, Y. Xiang, B.C. Sun, J.F. Chen, Micromixing efficiency of a novel helical tube reactor: CFD prediction and experimental characterization, *Chem. Eng. Sci.* 155 (2016) 386–396.
[27] Q.A. Wang, J.X. Wang, W. Yu, L. Shao, G.Z. Chen, J.F. Chen, Investigation of micromixing efficiency in a novel high-throughput microporous tube-in-tube microchannel reactor, *Ind. Eng. Chem. Res.* 48 (10) (2009) 5004–5009.
[28] N.C. Jacobsen, O. Hinrichsen, Micromixing efficiency of a spinning disk reactor, *Ind. Eng. Chem. Res.* 51 (36) (2012) 11643–11652.
[29] J.Z. Luo, G.W. Chu, Y. Luo, M. Arowo, B.C. Sun, J.F. Chen, Regulating the micromixing efficiency of a novel helical tube reactor by premixing behavior optimization, *AIChE J.* 63 (7) (2017) 2876–2887.
[30] L. Liu, X.G. Yang, Y.Q. Guo, B. Li, L.P. Wang, Reactive mixing performance for a nanoparticle precipitation in a swirling vortex flow reactor, *Ultrason. Sonochem.* 94 (2023) 106332.
[31] B.Q. Liu, N. Sun, Z.J. Jin, Y.K. Zhang, B. Sunden, Numerical investigation and estimating correlation of micromixing performance of coaxial mixers, *Ind. Eng. Chem. Res.* 58 (49) (2019) 22376–22388.
[32] M.C. Fournier, L. Falk, J. Villermaux, A new parallel competing reaction system for assessing micromixing efficiency – Determination of micromixing time by a simple mixing model, *Chem. Eng. Sci.* 51 (23) (1996) 5187–5192.
[33] M.C. Fournier, L. Falk, J. Villermaux, A new parallel competing reaction system for assessing micromixing efficiency – Experimental approach, *Chem. Eng. Sci.* 51 (22) (1996) 5053–5064.
[34] D.A. Palmer, R.W. Ramette, R.E. Mesmer, Triiodide ion formation equilibrium and activity coefficients in aqueous solution, *J. Solut. Chem.* 13 (9) (1984) 673–683.
[35] J.H. Guo, Y.D. Liu, G.X. Shan, H.J. Li, W. Li, H.Y. Qin, J.K. Xia, J. Wu, J.L. Zhang, The structure-effect relationship between inline high shear mixers and micromixing: Experiment and CFD simulation, *Chem. Eng. Sci.* 272 (2023) 118605.
[36] P.Y. Wang, The model constant A of the eddy dissipation model, *Prog. Comput. Fluid Dyn. Int. J.* 16 (2) (2016) 118–125.
[37] E. Gavi, D.L. Marchisio, A.A. Barresi, CFD modelling and scale-up of confined impinging jet reactors, *Chem. Eng. Sci.* 62 (8) (2007) 2228–2241.